Tetrahedron 67 (2011) 3395–3405

Contents lists available at ScienceDirect

Tetrahedron

journal homepage: www.elsevier.com/locate/tet

Novel 2,7-substituted pyrene derivatives: syntheses, solid-state structures, and properties

Yali Qiao [a,b], Jing Zhang [a,b], Wei Xu [a,*], Daoben Zhu [a,*]

[a] Beijing National Laboratory for Molecular Sciences, Organic Solids Laboratory, Institute of Chemistry, Chinese Academy of Sciences, Beijing 100190, PR China
[b] Graduate School of Chinese Academy of Sciences, Beijing 100049, PR China

ARTICLE INFO

Article history:
Received 24 January 2011
Received in revised form 7 March 2011
Accepted 17 March 2011
Available online 25 March 2011

Keywords:
2,7-Substituted pyrene
Crystal structures
Density functional theoretical calculation
Field-effect transistors

ABSTRACT

A novel series of pyrene derivatives **3**–**6** functionalized with different aromatic substituents at 2,7-positions of the pyrene core have been readily synthesized by Suzuki coupling reactions. Single crystals suitable for X-ray crystallographic analysis of compounds **3**–**6** were all successfully obtained. The optical, electrochemical, and thermal properties of these newly synthesized compounds were thoroughly investigated and discussed. Theoretical calculation was adopted to study the geometric and electronic structure of compounds **3**–**6**. Additionally, preliminary studies demonstrated that field-effect transistors using compound **3**, **5**, and **6** performed as p-type semiconductors, in which a field-effect mobility as high as 0.018 $cm^2 V^{-1} s^{-1}$ and current on/off ratio of 10^6 were achieved from compound **6**.

1. Introduction

Organic field-effect transistors (OFETs) have been intensively investigated[1–3] since first reported in 1986.[4] In comparison with the conventional inorganic silicon-based transistors, devices based on organic semiconductors have several advantages according to their low weight, high flexibility, and various ways of easy processability[5,6] for realization of low-cost fabrication on large-area and flexible substrates. In addition, the optical and electronic properties of organic semiconductors can be intentionally tuned by rationale design and synthesis. Consequently, organic FETs show potential for use in a number of novel electronics applications,[7–11] such as identification (ID) tags and smart cards,[12,13] electronic papers and displays,[14–17] sensors,[18,19] and so on.

Among p-type organic semiconductors, pentacene has been considered as a landmark, which exhibits outstanding charge carrier mobility applied in OFETs.[20,21] Additionally, many functionalized pentacene derivatives[22,23] and sulfur-containing acenes[24,25] were synthesized and successfully applied in OFETs. Corresponding to these linearly π-conjugated acenes, there are some *peri*-annulated hydrocarbons[26,27] materials, for which few attention has paid on, especially the systematic studies on structure–property relationship for such materials. As one of the smallest *peri*-annulated hydrocarbons, pyrene displays remarkable π-stacking both in solution and in the solid state.[28] Such ordered molecular arrangement is usually considered to be favorable for efficient charge transport when applied in OFETs. Recently, some substituted pyrene derivatives (e.g., 1,3,6,8-tetrathienylpyrene,[29] 1,6- or 1,8-dithienylpyrene,[30] and so on) have been synthesized and used as active layers in organic thin film or single crystal FETs with moderate charge mobility.[31] However, as the best of our knowledge, design and synthesis of pyrene derivatives functionalized at 2,7-position to explore the electrical transport properties and structure–property relationship have not been reported yet.

In this article, we report the synthesis and characterization of a series of novel 2,7-substituted pyrene derivatives. All the four targeting molecules **3**–**6** (Scheme 1) were readily synthesized in only one step by classical Suzuki coupling reaction between the pyrene-bis(boronate) ester[32] and corresponding aryl- or heteroaryl-bromide in moderate yields. All compounds exhibit good thermal and oxidative stability in air. Substitution at 2,7-positions of parent pyrene, other than at 1-, 3-, 6- or 8-position, is expected to provide larger space for substituent and reduce the sterically induced twist between the substituent and adjacent aromatic ring. Thus, such molecular structure will improve the planarity over the whole molecules and enhance the π–π interactions in the solid state, which are favorable for effective charge transport in OFET. Moreover, variation of the substituent provided the opportunity for exploring the molecular structure–property relationship in detail.

* Corresponding authors. Tel.: +86 10 6263 9355; fax: +86 10 6256 9349 (W.X.); tel.: +86 10 6254 4083; fax: +86 10 6256 9349 (D.Z.); e-mail addresses: wxu@iccas.ac.cn (W. Xu), zhudb@iccas.ac.cn (D. Zhu).

0040-4020/$ – see front matter © 2011 Elsevier Ltd. All rights reserved.
doi:10.1016/j.tet.2011.03.055

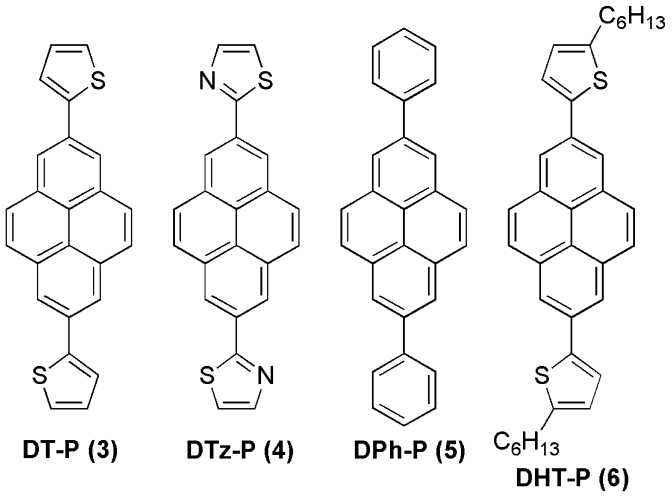

Scheme 1. Structures of 2,7-substituted pyrene derivatives.

2. Results and discussion

2.1. Synthesis

The 2,7-substituted pyrene derivatives **3**–**6** were synthesized following the synthetic route outlined in Scheme 2. The direct borylation of pyrene at the 2 and 7 positions was produced with Ir-based catalyst, which was prepared in situ via reaction of [Ir(OMe)COD]$_2$ with 4,4′-di-*tert*-butyl-2,2′-bipyridine (dtbpy) according to the previous report.[32] The syntheses of the present compounds **3**–**6** were realized by ordinary Suzuki coupling reactions of the pyrene boronate ester with different bromo-substituted (hetero)aryl rings in moderate yields. All the products are soluble in common organic solvents, such as CH_2Cl_2, $CHCl_3$, THF, and toluene, thus allowing these materials to be easily purified by a combination of column chromatography and recrystallization. Therefore, the compounds were fully characterized by EIMS, ^{1}H NMR, ^{13}C NMR, elemental analysis. Besides, the single crystals of the four compounds suitable for X-ray structure analysis are obtained, which is favorable for exploring the structure–property relationship. Thermal properties investigated by thermal gravimetric analysis (TGA, see Fig. S1) indicate that all the compounds have very good thermal stabilities. To the best of our knowledge, all the target 2,7-diaryl pyrene derivatives were prepared for the first time.

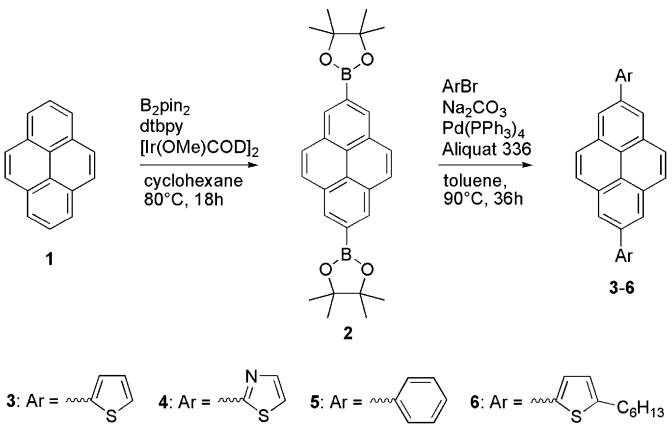

Scheme 2. Synthesis of the derivatives **3**–**6**.

2.2. Crystal structure analysis

Single crystals of all the pyrene derivatives **3**–**6** suitable for X-ray crystallographic analysis were gained by two different methods. For compounds **3**, **4**, and **6**, the single crystals were obtained by slow evaporation of the corresponding solutions. In the case of compound **5**, physical vapor transport (PVT) method was employed to obtain the single crystal. Here, we report the molecular and packing structures of the four crystals. All of the 2,7-substituted pyrene derivatives possess at least one common symmetry factor, that is, an inversion center located at the center of the pyrene core. Additionally, there is a dihedral angle existing between the substituent ring and the parent pyrene plane for all the derivatives. For compounds **3**, **4**, and **6**, the molecules are almost coplanar with a dihedral angle around or less than 10°, whereas diphenyl-substituted derivative **5** deviates significantly from planarity (a dihedral angle>30°). Moreover, the X-ray analysis demonstrates that variation of substituent has a significant influence on not only the molecular structure but also the solid-state packing pattern.

Single crystal of compound **3** was obtained from a dichloromethane solution and the molecular and crystal structures are displayed in Fig. 1. Compound **3** crystallizes in a monoclinic system and belongs to the *C*2/*c* space group with unit-cell parameters: a=21.662 (4) Å, b=4.0056 (8) Å, c=21.773 (4) Å, β=117.65 (3)°. The thiophene units are disordered over two positions related by a 180°

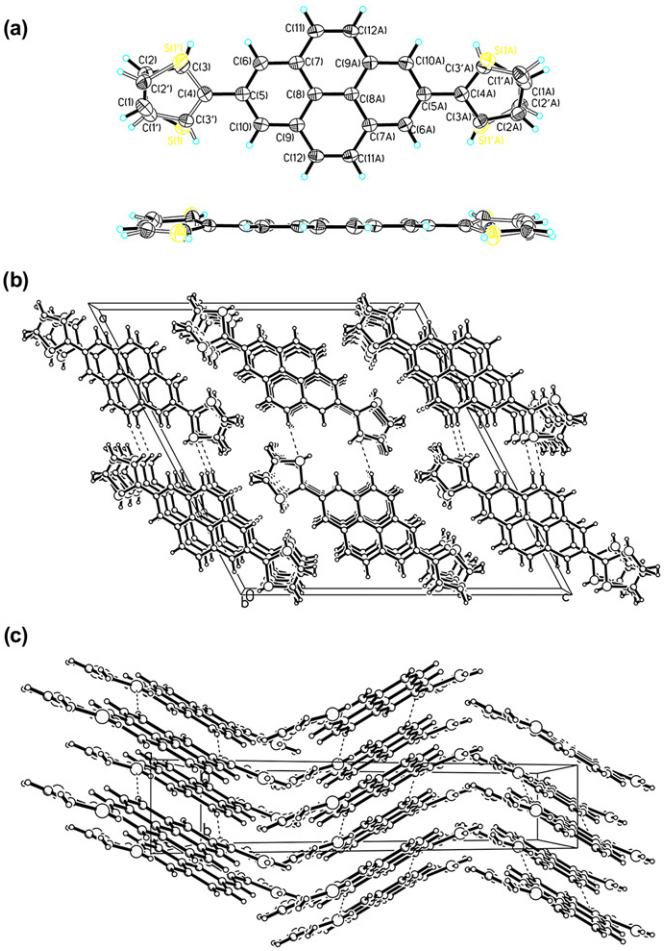

Fig. 1. X-ray crystal structure of compound **DT-P** (**3**): (a) molecular structure with 50% probability ellipsoids. (b) Packing structure view along *b*-axis (dash lines indicating the no bonding interactions), and (c) view along the *a*-axis.

rotation about C4–C5 bond. According to the references, the thienyl substituents are usually connected to the flat pyrene core with a larger twisted angle (ca. 40–60°) in 1,3,6,8-tetrathienylpyrene and 1,6-/1,8-dithienylpyrene. However, in case of 2,7-dithienylpyrene **3**, the molecules possess an almost coplanar structure with a dihedral angle of 10.891 (208)° between the pyrene core and the thienyl plane (Fig. 1a), revealing a remarkably improved coplanarity over the whole molecule and suggesting that the coplanarity between the substituent and the pyrene core could be modified by rationale adjustment of the substitution position at pyrene core for such thienyl-substituted pyrene derivatives. As shown in Fig. 1b, the molecules pack into columns along the *b*-axis uniformly and present shifted face-to-face patterns between adjacent molecules with an interplanar distance between pyrene cores of 3.4392 Å, indicative of the existence of π–π interaction. The neighboring packing columns are associated with each other by twofold screw axis with direction along *a*-axis and S···H–C hydrogen bonds exist between columns (Fig. 1c).

Single crystal of compound **4** was crystallized from a toluene/dichloromethane mixed solution. Both the molecular and crystal structures of it are quite similar to those of compound **3** as shown in Fig. 2. Just as compound **3**, compound **4** also crystallizes in a monoclinic system. However, it belongs to the $P2_1/n$ space group with unit-cell parameters: a=3.8727 (8) Å, b=20.191 (4) Å, c=10.540 (2) Å, β=99.48 (3)°. The thiazole units are disordered over two positions related by a 180° rotation about C4–C9 bond. As shown in Fig. 2a, the planarity of molecules for compound **4** slightly improved with a smaller dihedral angle of 7.07 (12)° between the pyrene core and the thiazole ring compared with compound **3**. As in Fig. 2b, the molecules also stack in a uniform style adopting a slipped face-to-face π-stacking pattern along the *a*-axis with an interplanar distance between pyrene cores of 3.4288 Å, which reduced a little in comparison with compound **3** and thus might account for the slight conformational variation (decrease of dihedral angle by ca. 3.891°). Such a bit reduction of the distance suggests comparable π–π interactions for the two compounds. Besides, the molecules loosely resemble the herringbone packing manner within the *ab* layer (Fig. 2c) as usually observed in acenes, such as pentacene.[33,34] Furthermore, twofold screw axis also exists along *b*-axis and weak no bonding interaction is observed between adjacent columns.

Single crystal of compound **5** was obtained by PVT method. It crystallizes in an orthorhombic system and belongs to the *Pbca* space group with unit-cell parameters: a=7.7673 (16) Å, b=7.6033 (15) Å, c=30.732 (6) Å. As in Fig. 3a, molecules apparently deviate from planarity with a larger dihedral angle of 33.253 (56)°, which is mainly owing to the steric hindrance between the hydrogen atoms on the phenyl substituent and pyrene core. From Fig. 3b, it can be seen that the molecules uniformly pack into a two dimensional layer structure along *ac*-plane. In one layer the molecules form a face-to-edge herringbone packing but with a dihedral angle of 36.024° between adjacent molecules along *b*-axis (Fig. 3c). Furthermore, two kinds of short C–H···π (2.806 Å and 2.814 Å)

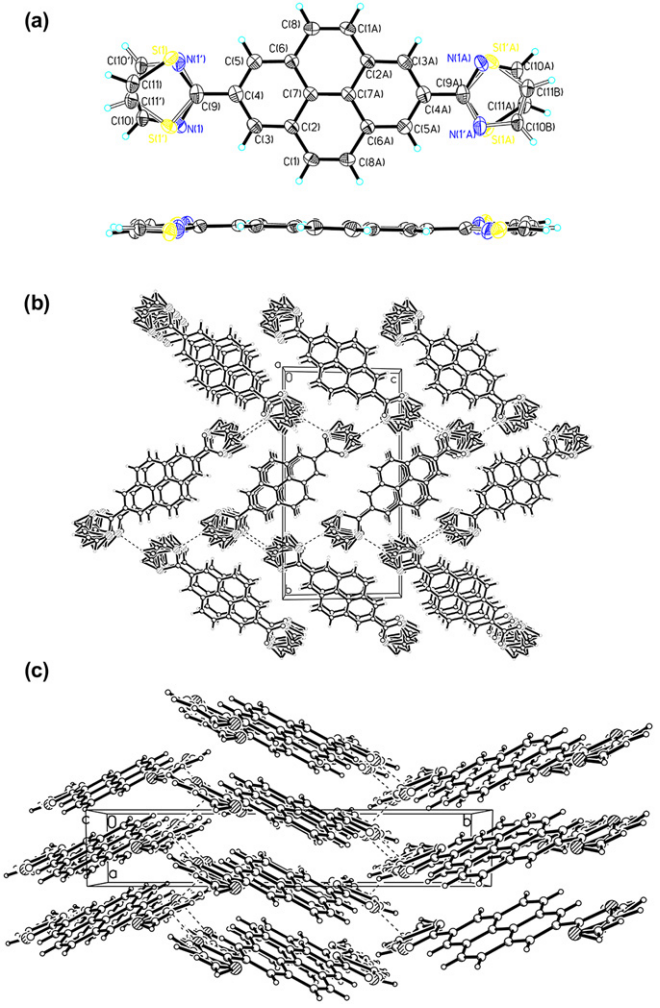

Fig. 2. X-ray crystal structure of compound **DTz-P** (**4**): (a) molecular structure with 50% probability ellipsoids. (b) Packing structure view along *a*-axis, and (c) view along the *c*-axis.

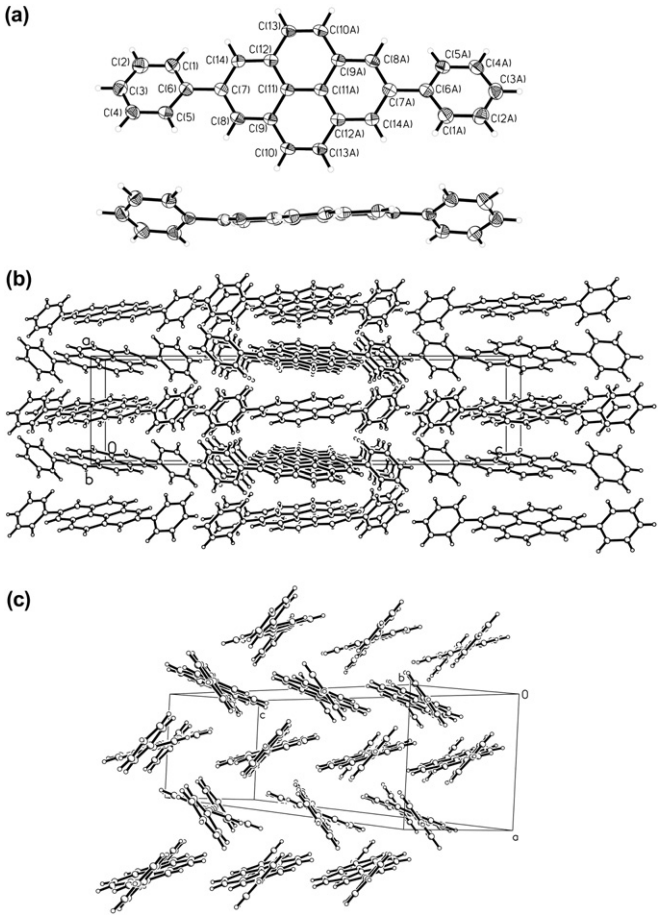

Fig. 3. X-ray crystal structure of compound **DP-P** (**5**): (a) molecular structure with 50% probability ellipsoids. (b) Layer packing structure view along *b*-axis, and (c) herringbone pattern in one stacking layer.

nonbonding interactions were found along *a*-axis within the same plane (see Fig. S4).

Single crystal of compound **6** gained from dichloromethane solution crystallizes in a triclinic system and belongs to the *P*−1 space group with unit-cell parameters: a=5.727 (2) Å, b=7.821 (4) Å, c=16.117 (7) Å, α=93.601 (6)°, β=91.506 (9)°, γ=103.674 (7)°. For the molecular structure of **6** in Fig. 4a, the dihedral angle is only 6.943 (26)° between the hexyl end-capped thienyl ring and the pyrene core, which decreases by ca. 3.948° than that of compound **3** and becomes the smallest one for this class of pyrene derivatives. Similarly, the molecules uniformly stack into columns along *a*-axis. However, the distance between two adjacent overlapped molecules is only approximately 3.1718 Å, which is the shortest interlayer distance among all the derivatives, however the degree of intermolecular overlapping is quite small as shown in Fig. 4c. When viewed along *c*-axis (Fig. 4c), it is significantly notable that the molecules arrange in a parallel packing motif with an offset face-to-face structure, which is totally distinct from the other derivatives. In addition, short C–H···π (2.831 Å) intermolecular interactions between the hexyl side chain and the pyrene core exist within the *ab* plane (see Fig. S3), which further contributes to form a compressed packing pattern.

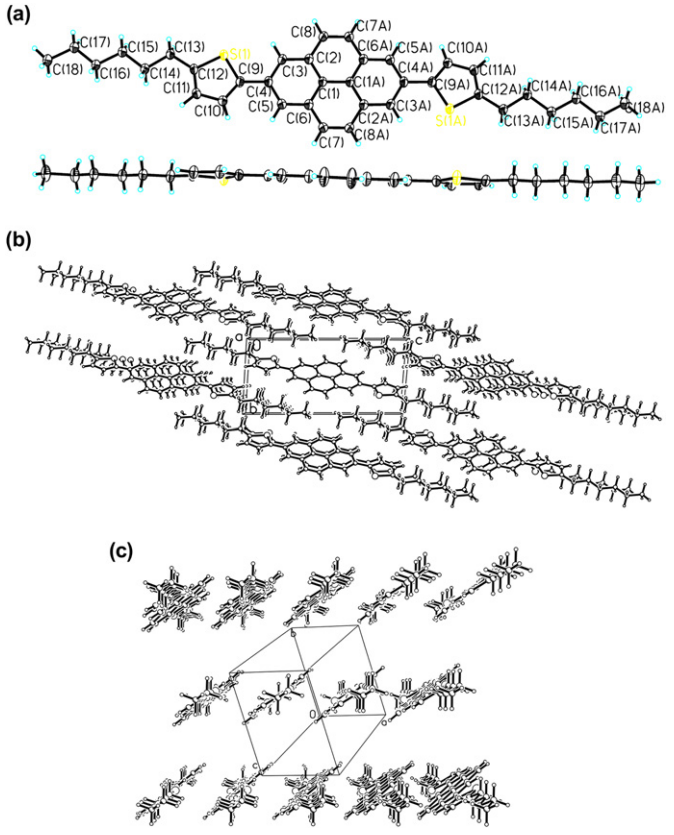

Fig. 4. X-ray crystal structure of compound **DHT-P** (**6**): (a) Molecular structure with 50% probability ellipsoids. (b) Packing structure view along *a*-axis, and (c) shifted face-to-face stacking pattern.

2.3. Photophysical properties

The data of photophysical properties for compounds **3**–**6** and pyrene both in solutions and in solids are summarized in Table 1. The UV–vis absorption spectra of the derivatives **3**–**6** in dilute dichloromethane solutions (1.0×10^{-5} M) with that of the parent compound pyrene for comparison are displayed in Fig. 5. All the derivatives exhibited similar absorption behavior with well-defined vibronic π–π* transition absorption bands, which probably derived from the similar molecular structures with pyrene as the core. The spectrum of pyrene in dilute solution showed two major absorption bands with maximum absorption wavelength at about 274 and 336 nm, respectively. For the latter one, three vibronic bands were apparently observed at 307 (32,573 cm^{-1}), 321 (31,153 cm^{-1}), and 336 nm (29,762 cm^{-1}), indicating that the vibrational energy levels in the excited state of pyrene appeared to be equally separated with a wavenumber separation of about 1420 cm^{-1}. Consequently, it is expected that the three vibronic bands of pyrene at 336, 321, and 307 nm were probably corresponding to 0–0, 0–1, and 0–2 transitions,[26] respectively. However, all of 2,7-substituted derivatives **3**–**6** exhibited multiple overlapping absorption bands and thus such similar characteristic vibronic bands could only be easily distinguished for compound **5**. In the spectrum of **5**, the vibronic bands at about 342, 326, and 313 nm were accordingly corresponding to 0–0, 0–1, and 0–2 transitions, respectively. All the three bands were slightly red-shifted (5–6 nm) in comparison with pyrene as a reflection of slight extension of the effective conjugation length with the introduction of phenyl substituent. In addition, a very broad and intense absorption band appeared with absorption λ_{max} at about 291 nm due to the π–π* transitions originating from both the phenyl substituent and the parent pyrene moiety. With the exception of **5** with

Table 1
Photophysical, electrochemical, and thermal properties of **3**–**6** in comparison with pyrene

Compd	λ_{abs} (nm) (ε, M^{-1} $cm^{-1}\times10^3$) soln[a]	λ_{abs} (nm) film[b]	λ_{em} (nm) soln[a]	Stokes shift (nm)[c]	Φ_f[d]	E_{ox} (V)	E_{ox}^{onset} (V)	HOMO (eV)[e]	T_d (°C)[f]	T_m (°C)[g]
3	309 (76.9), 318 (83.6), 339 (43.4), 355 (9.2), 386 (0.5)	332, 348	431, 447	76	0.025	1.32	1.21	−5.61	332	298
4	309 (84.9), 318 (98.3), 338 (54.8), 352 (19.4), 405 (0.5)	329	428, 452, 483	76	0.075	1.53, 1.82	1.30	−5.70	356	303
5	291 (91.6), 313 (23.8), 326 (19.9), 342 (34.9)	313, 344 352	415, 431, 463	73	0.006	1.56	1.35	−5.75	338	316
6	310 (73.4), 322 (111.5), 340 (76.6), 358 (27.9), 387 (1.2)	330	437, 458	79	0.026	1.42, 1.76	1.15	−5.55	387	228
Pyrene	263(21.6), 274 (37.1), 307 (11.4), 321 (24.7), 336 (38.5)	—	378, 388	42	0.28	—	—	—	—	—

[a] Measured in dilute dichloromethane (ca. 1×10^{-5} M).
[b] Measured from vacuum-deposited film.
[c] Calculated from the absorption and emission wavelengths in dichloromethane solution.
[d] Φ_f of compounds **3**–**6** and pyrene were measured in dichloromethane using anthracene (in hexane, Φ_f=0.31) as reference.
[e] Estimated from the empirical equation $E_{HOMO}=-(4.40+E_{ox}^{onset})$ eV.
[f] Measured at nitrogen atmosphere with a heating rate of 10 °C/min.
[g] Derived from DSC measurement at nitrogen atmosphere with a heating rate of 10 °C/min (see Fig. S2).

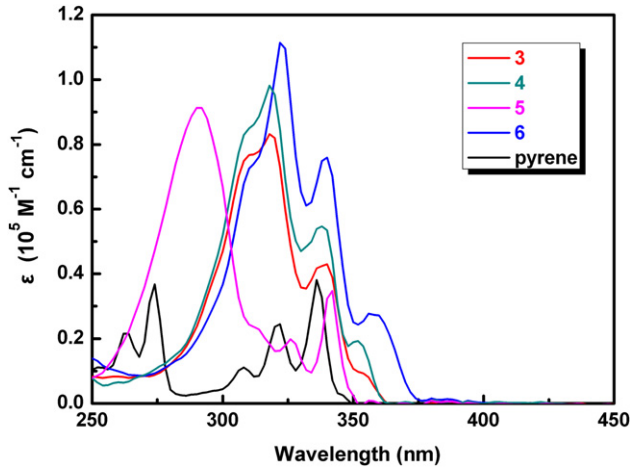

Fig. 5. Absorption spectra of **3**–**6** and pyrene in dilute dichloromethane solution (1×10^{-5} M).

phenyl as substituent, derivative **3**, **4**, and **6** displayed much more similar absorption behavior due to the analogous heterocyclic five-member ring substitution. In the spectra of compounds **3**, **4**, and **6**, the multiple absorption bands were much more overlapped with absorption λ_{max} at the range of 318–322 nm, which was bathochromically shifted intensively compared to pyrene by 44–46 nm and even phenyl-substituted derivative **5** by 27–31 nm. The large red-shift manifested the intensive increase of coplanarity over the whole molecule when the heterocyclic five-member ring was used as substituent, and the resulting further extension of the effective conjugation length. Besides, we could observe that the λ_{max} in dilute CH_2Cl_2 solution of the hexyl end-capped thiophenepyrene oligomer **6** was slightly red-shifted (4 nm) with respect to that of compound **3** (without hexyl group), which is similar to the phenomenon previously reported for the oligothiophenes.[35]

Fig. 6 showed the emission spectra of the derivatives **3**–**6** and pyrene in dilute dichloromethane solutions (1.0×10^{-5} M). As for pyrene, the emission peaked at 378 and 388 nm with almost identical intensity. The emission λ_{max} of compound **5** mainly peaked at 415 and 431 nm with a concomitant reduction of the intensity of the lower energy peak. Both the emission peaks intensively red-shifted (37–45 nm), which is in good agreement with

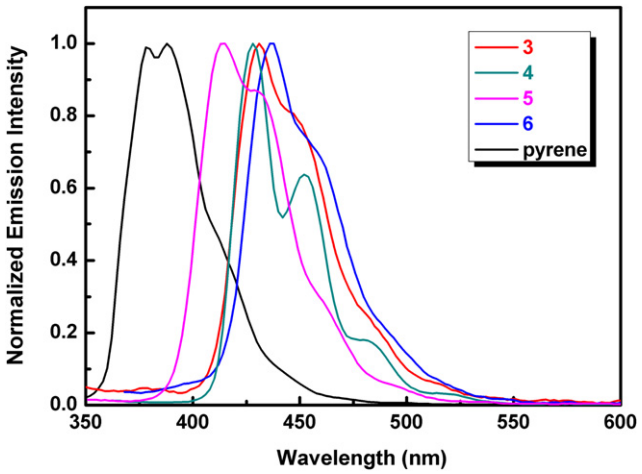

Fig. 6. Emission spectra of **3**–**6** and pyrene in dilute dichloromethane solution (1×10^{-5} M). The emission spectra were recorded using the following excitation wavelength: 339 nm for **3**; 352 nm for **4**; 341 nm for **5**; 358 nm for **6**, and 336 nm for pyrene.

the phenomenon appeared in absorption spectra and also ascribable to the introduction of phenyl substituent when compared to pyrene. Derivative **3** and **6** displayed almost the same emission behavior as **5**, with the emission peak of **6** (437 and 458 nm) slightly red-shifted of 6–11 nm in comparison with **3** (431 and 447 nm) as observed in the absorption spectra. Unlike the asymmetric broadening emission bands for **3**, **5**, and **6**, the emission spectrum of **4** exhibited an obvious vibronic pattern with three emission peaks at 428, 452, and 483 nm. Besides, it was observed that all heterocyclic five-member ring substituted oligomers **3**, **4**, and **6** bathochromically shifted much more than phenyl ring substituted derivative **5** when compared to parent pyrene. The results are in accordance with the red-shift observed in absorption spectra and further reveal the different extent of π-conjugation extension over the molecule. In addition, all derivatives showed one or two orders of magnitude lower quantum yields than that of parent pyrene. The relatively low quantum yields observed for the derivatives might be mainly stemmed from the nonradiative deactivation for the excited state.

As showed in Fig. 7, we also investigated the UV–vis spectra of derivatives **3**–**6** in thin films (with a film thickness of ca. 50 nm) vacuum-deposited on quartz glass in comparison with those in the dilute solution. For all the derivatives, the absorption λ_{max} in the solid state became broadened and red-shifted more or less with regard to those in solutions. This phenomenon was easily understood and mainly ascribed to the much stronger intermolecular interaction between molecules in the solid states, which could induce the reduction of the energy of the exciton.

2.4. Electrochemical properties

Fig. 8 displays the cyclic voltammograms of derivatives **3**–**6**, which were carried out in dichloromethane with 0.1 M tetrabutylammonium hexafluorophosphate as the electrolyte in a conventional three-electrode cell. Ferrocene/ferrocenium (Fc/Fc^+) was adopted as an internal potential marker in order to calibrate the redox potentials. All the derivatives showed one or two irreversible oxidation peaks, which are in a relatively high potential range (ca. +1.32–1.56 V vs Ag/AgCl) without observation of any reduction processes. Two irreversible oxidation peaks were observed for derivatives **4** and **6** and the appearance of the second oxidation process could be owing to the effective intension of π-conjugation range over the whole molecule.[30] Although the first oxidation potential peak decreases as following: **5**>**4**>**6**>**3**, the onset potentials of first oxidation for **6** are cathodically shifted than **3** (E_{ox}^{onset}: **5**>**4**>**3**>**6**). This tendency reflects the more enhancement of the electron-donating capability when substituted by heteroaromatic five-ring than phenyl substituent. In particular, hexyl end-capped thiophenepyrene **6** exhibited lower oxidation onset than that of the derivative without hexyl side chain, resulting from the electron-donating nature of the alkyl side chains. The highest occupied molecular orbital (HOMO) energy value could be determined from the onset oxidation potential by using the equation HOMO=−(E_{ox}^{onset}+4.40) eV.[36] As a result, the onset potentials for oxidation of **3**–**6** were 1.21 eV, 1.30, 1.35 eV, and 1.15 eV, corresponding to the estimated HOMO levels as −5.61 eV, −5.70 eV, −5.75 eV, and −5.55 eV, respectively. The HOMO levels were relatively low-lying, which should indicate better stability against oxygen under ambient conditions. However, such low-lying HOMO energy levels might enhance the barrier for the injection of holes from electrodes to active semiconductor layers.

2.5. Theoretical investigations

To gain insight into the electronic structure and transition energies of these pyrene derivatives, quantum-chemical calculations

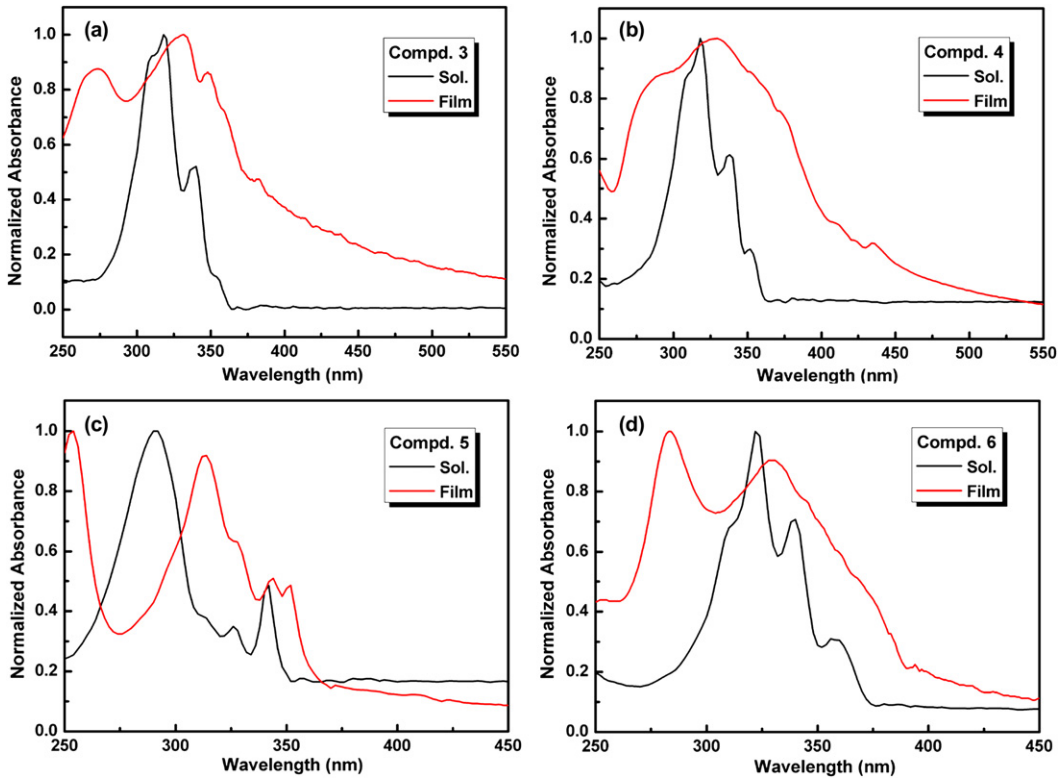

Fig. 7. UV–vis spectra of compounds **3**–**6** in dilute solution and solid state (vacuum-deposited films of 50 nm thickness on quartz glass).

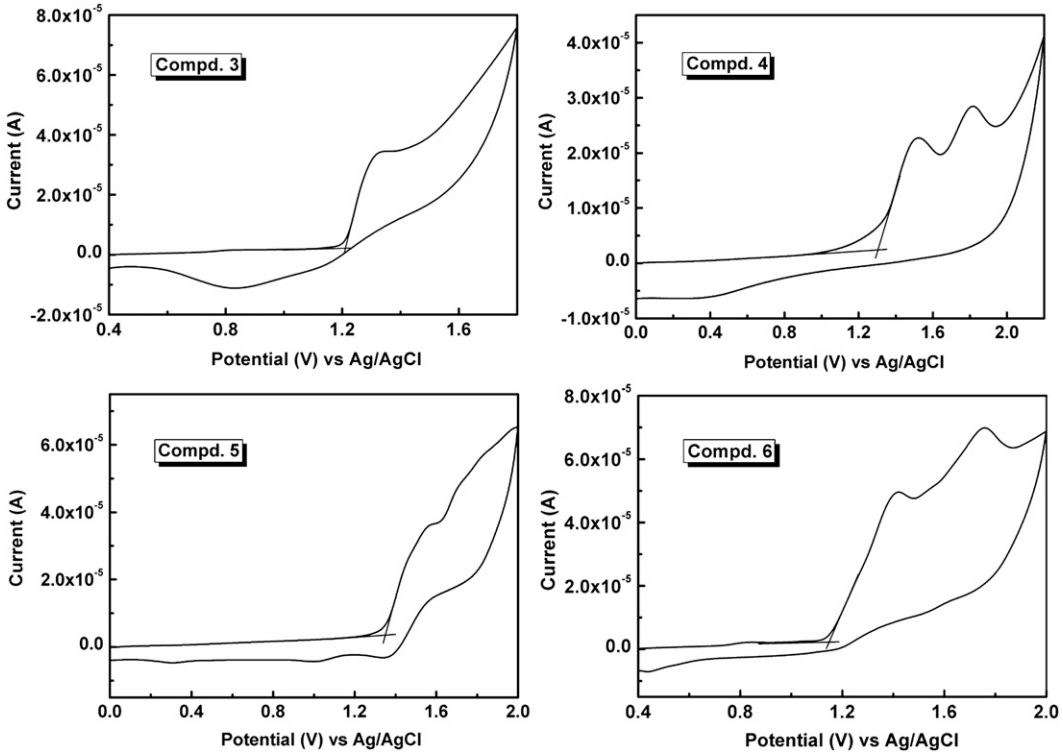

Fig. 8. Cyclic voltammograms of compounds **3**–**6** in dilute solution (1×10^{-5} M). Scan rate, 100 mV s^{-1}; working electrode, Pt; counter electrode, Pt wire; reference electrode, Ag/AgCl; supporting electrolyte, Bu_4NPF_6 (0.1 M). Fc/Fc^+ was used as the internal reference ($E_{1/2}$=+0.43 V measured under identical conditions).

were performed using the Gaussian 03 package.[37] The atomic coordinates obtained from the crystal structure were used as the initial guess structure and optimized fully by the DFT method in the gas state using B3LYP functional with 6-31G* basis sets. Time-dependent DFT (TDDFT) calculations were employed to analyze the vertical transition energies, oscillator strengths, and electronic configurations for low-lying singlet excited states.

Fig. 9 illustrates the theoretically simulated frontier molecular orbitals in the ground states for the 2,7-substituted pyrene derivatives **3**–**6** with pyrene together. For compound **5**, the

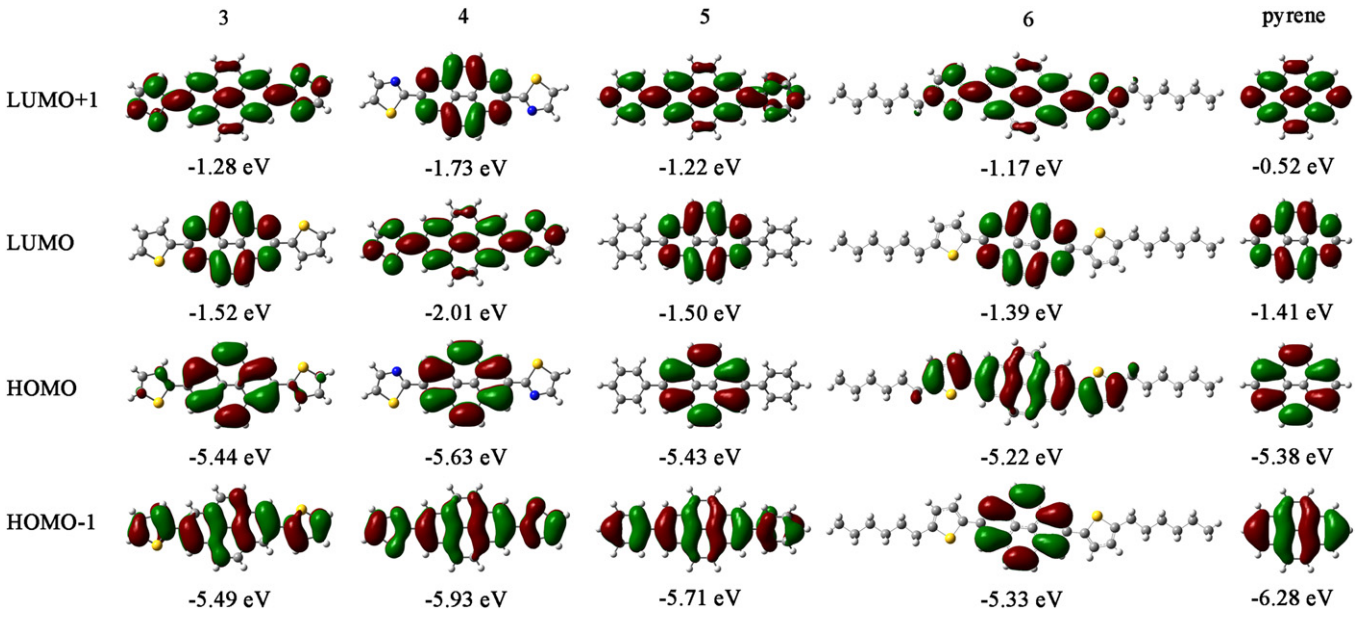

Fig. 9. Frontier molecular orbital densities for the 2,7-substituted pyrene-based derivatives **3**–**6** and pyrene as determined with TDDFT at the B3LYP/6-31G* level of theory.

introduction of phenyl group does not make any change to the molecular frontier orbital (HOMO and LUMO) distribution of the electron density, just essentially the same as the parent compound pyrene. However, some changes have taken place for the frontier orbital (HOMO or LUMO) distribution of the electron density to the other five-membered heterocyclic ring substituted derivatives **3**, **4**, and **6**. For compound **3**, the HOMO orbital distribution of the electron density partially extended to the thiophene substituents, whereas the shape of HOMO orbital distribution of the electron density for derivative **6** alters a lot and is spread to the whole thiophene substituents even to the first carbon atom of the hexyl side chain. In fact, hexyl end-capped thiophenepyrene **6** possesses the highest HOMO energy level among all the derivatives not only from a theoretical point of view but also revealed experimentally by the electrochemical and optical studies. Unlike **3** and **6**, the HOMO of thiazole substituted compound **4** is contributed totally by the parent pyrene moiety. In addition, the LUMO is extended over the whole molecule and thus compound **4** becomes the one with the lowest LUMO energy level among this series, which may be ascribable to the electron-deficient nature of the thiazole substituent and is in good agreement with the experimental results.

The HOMO, LUMO energy levels, and HOMO–LUMO energy gap calculated for the derivatives **3**–**6** and pyrene are summarized in Table 2. The HOMO energy levels of the derivatives **3**–**6** vary in a range from 5.22 to 5.63 eV (below the vacuum) with the hexyl end-capped thiophenepyrene **6** having the highest HOMO level (5.22 eV) as revealed experimentally. On the other hand, the LUMO energy levels emerge in the range of 1.39–2.01 eV with the thiazolepyrene **4** occupying the most stable LUMO level (2.01 eV). Besides, all the derivatives possess large energy gaps coupled with their low-lying HOMO energy levels, indicative of good stabilities against oxygen under ambient conditions. For this series of derivatives, the rather high LUMO energy levels indicate that these molecules could not be effective semiconductor layers for electron-transport because of the very large energy barrier existing for electron injection from the electrode to the organic layer. However, both theoretical and experimental HOMO energy levels of the derivatives suggest that it is probably effective for hole-transport by hole injection from the metal electrode (Au with a work function of ca. 5.1 eV) to the active layer.

Furthermore, considering the direct correlationship between the energy levels/gaps of molecular frontier orbitals (HOMO and LUMO) and the optical properties for compounds, excited-state vertical transitions for all the derivatives **3**–**6** and pyrene were calculated with TDDFT method at the B3LYP/6-31G* level of theory. The vertical transition wavelengths, oscillator strengths, and excited-state electronic configurations in each molecule are listed in Table 2, and the simulated UV–vis absorption spectra of all the derivatives from the computed parameters and an average full-width at half-maximum of 1800 cm^{-1} are presented in Fig. 10. For each of compounds **3**, **4**, and **6**, the lowest energy electronic transition (380–410 nm) is theoretically corresponding to the electronic configuration, which primarily includes electronic excitations from the HOMO to the LUMO with very small oscillator strength. Generally, electronic transition with so small intensity is difficult to be observed in the experimental characterizations. However, it is worth noting that there are really absorptions but with very poor intensity in the UV–vis spectra for compounds **3**, **4**, and **6** (Table 1), which is in well agreement with the theoretical calculations (Table 2). Furthermore, the higher energy absorption bands observed experimentally in the range of 310–360 nm could be ascribed to the multiple overlapping $\pi-\pi^*$ transitions, which are principally comprised of the electronic excitations involving configurations, such as HOMO−1 and LUMO+1. In addition, the lower energy absorption bands with the largest intensity are well simulated by the theoretical calculations for all the compounds.

2.6. Thin film transistors

OFET devices of pyrene derivatives **3**–**6** were fabricated in a top-contact configuration, in which the drain and source electrodes are deposited on top of the active layer. An n-type Si wafer with a SiO_2 layer of 500 nm thickness and a capacitance of 7.5 nF cm^{-2} was used as the gate. Thin films of 50 nm thickness based on the derivatives were vacuum-evaporated on octadecyltrichlorosilane (OTS) modified SiO_2/Si substrates at room temperature. Subsequently, gold electrodes were deposited by vacuum evaporation on the active layers through a shadow mask. The channel length (L) and width (W) were 0.11 mm and 5.30 mm, respectively. The OFETs measurements were performed under ambient atmosphere at room temperature using a semiconductor parameter analyzer. The OFET devices based on compound **4** did not show any FET performance. On the other hand, the OFET devices based on compounds

Table 2
Selected wavelengths (λ, nm), oscillator strengths (arbitrary units), excited-state electronic configurations, and orbital energies as determined with TDDFT at the B3LYP/6-31G* level of theory

Compd	λ_{opt} (nm)	f	Configuration	HOMO (eV)	LUMO (eV)	E_g (eV)
3	383.19	0.0024	HOMO→LUMO (41%)	−5.44	−1.52	3.92
	346.30	0.0286	HOMO→LUMO+1 (36%)			
			HOMO−1→LUMO (34%)			
			HOMO→LUMO (33%)			
	320.02	0.1012	HOMO→LUMO+1 (37%)			
			HOMO−1→LUMO+1 (36%)			
			HOMO→LUMO (24%)			
			HOMO−6→LUMO (10%)			
	306.18	2.2330	HOMO−1→LUMO+1 (34%)			
			HOMO→LUMO (29%)			
			HOMO−1→LUMO (28%)			
4	389.77	0.0149	HOMO→LUMO (60%)	−5.63	−2.01	3.62
			HOMO−1→LUMO+1 (36%)			
			HOMO→LUMO+1 (12%)			
	347.71	0.0818	HOMO−1→LUMO (51%)			
	317.91	0.1173	HOMO−1→LUMO+1(51%)			
	307.68	2.0926	HOMO→LUMO+1(39%)			
			HOMO−2→LUMO (36%)			
			HOMO−1→LUMO+1 (24%)			
			HOMO−2→LUMO+2 (10%)			
5	361.66	0.0016	HOMO−1→LUMO (52%)	−5.43	−1.50	3.93
	335.81	0.0636	HOMO→LUMO (57%)			
			HOMO−1→LUMO+1(34%)			
	286.75	2.3392	HOMO−1→LUMO+1 (58%)			
6	392.49	0.0051	HOMO→LUMO (59%)	−5.22	−1.39	3.83
			HOMO−1→LUMO+1 (39%)			
	352.97	0.3001	HOMO→LUMO+1 (56%)			
	328.08	0.0825	HOMO−1→LUMO+1 (55%)			
			HOMO−6→LUMO (12%)			
	317.70	2.3987	HOMO−1→LUMO (49%)			
			HOMO→LUMO+1 (35%)			
			HOMO−2→LUMO+2 (12%)			
Pyrene	328.58	0.2645	HOMO→LUMO (61%)	−5.38	−1.41	3.97
			HOMO−1→LUMO+1 (24%)			
	263.50	0.2557	HOMO−1→LUMO (44%)			
			HOMO→LUMO+1 (42%)			
			HOMO−3→LUMO+2 (16%)			

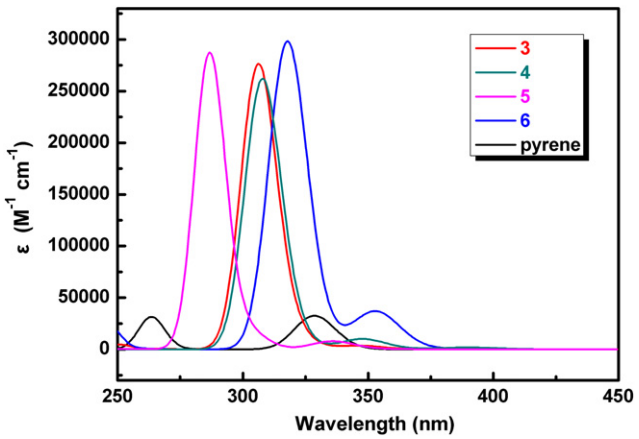

Fig. 10. Simulated electronic transitions for the compounds **3**–**6** and pyrene.

3, **5**, and **6** as active semiconducting layers exhibited p-type performance (see Fig. S5 for OFETs characteristic curves). Among them, compound **6** showed carrier mobility as high as 0.018 $cm^2 V^{-1} s^{-1}$ with a current on/off ratio of 10^6, and the threshold voltage was −39 V. In the case of compounds **3** and **5**, the carrier mobility was very similar (1.22×10^{-3} with on/off ratio of 10^6 and 1.19×10^{-3} $cm^2 V^{-1} s^{-1}$ with on/off ratio of 10^3 for **3** and **5**, respectively), both of which were one order of magnitude smaller than that of compound **6**. Additionally, the threshold voltages of compounds **3** and **5** are −43 V and −99 V, respectively. The results are in good agreement with the corresponding HOMO energy level order (E_{HOMO} under vacuum: **6**<**3**<**5**), which mainly determines the threshold voltage. To the best of our knowledge, these are the first class of 2,7-functionalized pyrene derivatives as effective p-type semiconducting layers applied in OFETs reported up to now.

The morphology and crystalline characteristics of the vacuum-deposited films of compounds **3**, **5**, and **6** on OTS modified SiO_2/Si at room temperature were investigated by atomic force microscopy (AFM) and X-ray diffraction (XRD), respectively, as depicted in Fig. 11. As showed in the AFM images (Fig. 11a–c), the three compounds have one characteristic in common, that is, the grains of the thin films all grow in a terrace pattern. The film for compound **6** is the most continuous one with grains growing along a screw direction. In the case of compound **3** and **5**, although the grains are much larger than that of compound **6**, the continuity is poor, especially for compound **3**, which possesses obvious intergrain boundaries and is expected to have a negative influence on the OFETs performance. On the other hand, all the thin films are polycrystalline as displayed in the XRD pattern (Fig. 11d–f). Notably, only the diffraction peaks of compound **5** can be indexed according to the single crystal structure (Fig. 11e). For compound **5**, the first peak appears at 5.8° with a *d*-spacing of 15.3 Å, corresponding to the thickness of a molecular monolayer. The molecular orientation on the substrate can be estimated by comparing the monolayer thickness with the actual molecular length; according to the molecular height (15.6 Å) derived from single crystal data, it is estimated that the molecules exhibit end-to-end packing on the substrate, resulting in an almost perpendicular arrangement of cyclic molecules on the dielectric surface upon deposition. However, for compounds **3** and **6**, the *d*-spacing of the first order peak revealed in XRD is smaller than the molecular height obtained from

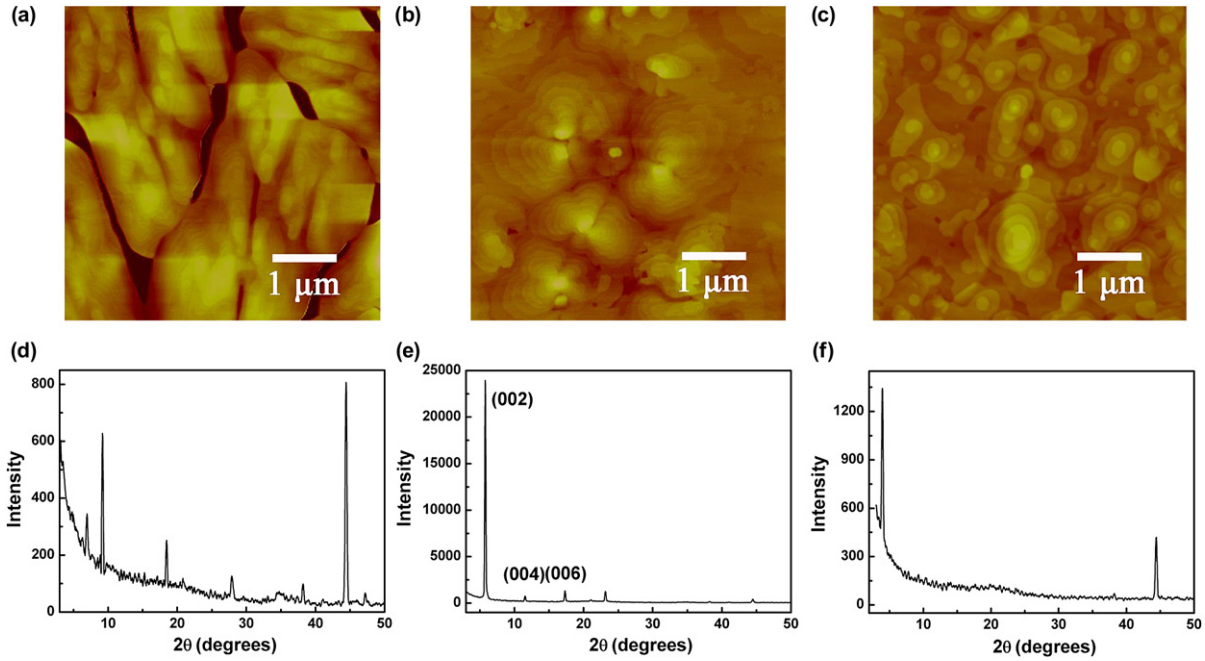

Fig. 11. AFM images and XRD patterns of 50-nm-thick thin films of compounds **3**, **5**, and **6** vacuum-deposited on OTS modified SiO_2/Si substrates at room temperature (20 °C): (a) and (d) for **3**; (b) and (e) for **5**; (c) and (f) for **6**. The scale of each AFM image is 5 μm×5 μm.

their single crystal structure, suggesting that the molecules tilt to the substrate.

3. Conclusion

In summary, we have facilely synthesized a novel series of 2,7-functionalized pyrene derivatives **3**–**6** by Suzuki coupling reaction. Single crystal X-ray analyses for all the derivatives demonstrate that the kind of substituent has a significant effect on both the molecular structure and the solid-state packing mode. Notably, 2,7-diphenylpyrene (**5**) arranges in a herringbone packing motif, whereas 2,7-di-(5-hexylthiophen-2-yl)-pyrene (**6**) arranges in a parallel packing motif. Besides, it is also worth noting that the planarity of the 2,7-dithienylpyrene **3** has been remarkably improved compared to 1,3,6,8-tetrathienylpyrene and 1,6-/1,8-dithienylpyrene reported previously, reflecting the position of substituent on the pyrene is another key factor contributed to the molecular structure. All the derivatives were further characterized by means of absorption spectroscopy, electrochemistry, quantum-chemical analysis, and employed as the active materials in organic TFTs. Through the preliminary research of the derivatives as active layers in OFETs by vacuum evaporation at room temperature, we found that compound **3**, **5**, and **6** performed as effective p-type semiconductors, in which a field-effect mobility as high as 0.018 $cm^2\ V^{-1}\ s^{-1}$ and current on/off ratio of 10^6 were achieved from compound **6**. Up to now, these are the first class of 2,7-functionalized pyrene derivatives as p-type semiconducting layers applied in OFETs. Further investigations of these materials in OFETs with optimized conditions and chemical modification of them to develop new pyrene derivatives for such application are now in progress in our laboratory.

4. Experimental section

4.1. General

All reagents and solvents were purchased from commercial suppliers and used directly as received unless otherwise stated. Anhydrous cyclohexane was purified with standard distillation procedures prior to use. Conventional Schlenk techniques were adopted and reactions were carried out under a nitrogen atmosphere unless otherwise stated. 2-Bromo-5-*n*-hexylthiophene and 2,7-$(bpin)_2$-pyrene (PB_2pin_2, **2**)[32] were synthesized according to literature procedures. ^1H NMR and ^{13}C NMR spectra were performed in $CDCl_3$ with TMS as internal standard on Bruker Advance 400 MHz spectrometers. MS (EI) measurements were performed on SHIMADZU GCMSQP2010 or UK GCT-Micromass spectrometers. Elemental analyses were measured on a Carlo Erba 1106 elemental analyzer.

4.2. General synthetic procedure for derivatives 3–6

To a solution of PB_2pin_2 (1.817 g, 4 mmol) and the corresponding bromo-substituted (hetero)aryls (9.6 mmol) dissolved in toluene (60 mL) was added a 2 M solution of sodium carbonate (2.12 g, 20 mmol) dissolved in water (10 mL). The mixture was bubbled with nitrogen for 30 min. Then, phase-transfer agent Aliquat 336 (0.91 mL) and tetrakis(triphenylphosphine)palladium(0) (0.46 g, 0.40 mmol) were added. The mixture was heated to 90 °C for 36 h under a nitrogen atmosphere. The resulting mixture was cooled to room temperature and poured into methanol (500 mL). The resulting precipitate was filtered off, washed with water, dilute acid (5% HCl), water, methanol, then with acetone to remove the starting material as well as the mono-substituted by-product. The crude product was purified by chromatography using petroleum/dichloromethane (2:1) as the eluent on a short column to give yellow powders followed by recrystallization from CH_2Cl_2/toluene to provide the desired product as crystals.

*4.2.1. 2,7-Di-(thiophen-2-yl)-4,5,9,10-tetrahydro-pyrene (**DT-P**, **3**).* Needle-like yellow crystals (0.25 g, 17%); mp 298 °C; IR (KBr) 3429, 3038, 1600 cm^{-1}. ^1H NMR (400 MHz, $CDCl_3$, ppm) δ 8.38 (s, 4H), 8.07 (s, 4H), 7.61 (s, 2H), 7.41 (d, 2H, J=4.9 Hz), 7.21 (s, 2H). ^{13}C NMR (100 MHz, $CDCl_3$, ppm): δ 144.9, 132.4, 131.7, 128.5, 128.1, 125.7, 124.1, 122.8. MS (EI, m/z): 366 (M^+). Anal. Calcd for $C_{24}H_{14}S_2$: C, 78.65; H, 3.85. Found: C, 78.26; H, 3.80.

*4.2.2. 2,7-Di-(thiazol-2-yl)-4,5,9,10-tetrahydro-pyrene (**DTz-P**, **4**).* Needle-like yellow crystals (0.5 g, 34%); mp 303 °C; IR (KBr) 3069,

3040, 1603 cm^{-1}. ^1H NMR (400 MHz, $CDCl_3$, ppm): δ 8.77 (s, 4H), 8.16 (s, 4H), 8.01 (d, 2H, J=3.0 Hz), 7.47 (d, 2H, J=3.0 Hz). ^{13}C NMR (100 MHz, $CDCl_3$, ppm): δ 168.7, 144.1, 131.9, 131.6, 128.4, 125.3, 123.3, 119.6. MS (EI, m/z): 368 (M^+). Anal. Calcd for $C_{22}H_{12}N_2S_2$: C, 71.71; H, 3.28; N, 7.60. Found: C, 71.62; H, 3.30; N, 7.45.

*4.2.3. 2,7-Diphenyl-4,5,9,10-tetrahydro-pyrene (**DPh-P**, **5**).* Pale yellow powders (0.56 g, 39%); mp 316 °C; IR (KBr) 3039, 1770, 1598 cm^{-1}. ^1H NMR (400 MHz, $CDCl_3$, ppm): δ 8.41 (s, 4H), 8.16 (s, 4H), 7.90 (d, 4H, J=7.5 Hz), 7.57 (t, 4H, J=7.6 Hz), 7.45 (t, 2H, J=7.4 Hz). ^{13}C NMR (100 MHz, $CDCl_3$, ppm): δ 141.7, 139.2, 131.7, 129.1, 128.2, 128.1, 127.6, 124.1, 124.0. MS (EI, m/z): 354 (M^+). Anal. Calcd for $C_{28}H_{18}$: C, 94.88; H, 5.12. Found: C, 94.48; H, 5.14.

*4.2.4. 2,7-Di-(5-hexylthiophen-2-yl)-4,5,9,10-tetrahydro-pyrene (**DHT-P**, **6**).* Yellow powders (0.56 g, 26%); mp 228 °C; IR (KBr) 3032, 2961, 2870, 2846, 1600 cm^{-1}. ^1H NMR (400 MHz, $CDCl_3$, ppm) δ 8.32 (s, 4H), 8.05 (s, 4H), 7.42 (d, 2H, J=3.4 Hz), 6.86 (d, 2H, J=3.1 Hz), 2.90 (t, 4H, J=7.6 Hz), 1.81–1.73 (m, 4H), 1.47–1.43 (m, 4H), 1.36–1.35 (m, 8H), 0.92 (t, 6H, J=6.5 Hz). ^{13}C NMR (100 MHz, $CDCl_3$, ppm): δ 146.7, 142.1, 132.6, 131.6, 128.0, 125.5, 123.9, 123.6, 122.3, 31.8, 31.7, 30.5, 29.0, 22.8, 14.2. MS (EI, m/z): 534 (M^+). Anal. Calcd for $C_{36}H_{38}S_2$: C, 81.38; H, 7.19. Found: C, 81.06; H, 7.16.

4.3. X-ray crystallographic analysis

X-ray crystallographic data were collected with a Bruker Smart CCD diffractometer through using graphite-monochromated Mo Kα radiation (λ=0.71073 Å). The data were collected at 173 K for compounds **4**–**6**, whereas the data for compound **3** was collected at 153 K. The structures were resolved by the direct method and refined by full-matrix least-squares on F^2. The computation was performed with the SHELXL-97 program. All non-hydrogen atoms were refined anisotropically. CCDC 808315 (**DT-P**), 808316 (**DTz-P**), 808317 (**DPh-P**), and 808318 (**DHT-P**) contain the supplementary crystallographic data for this paper. These data can be obtained free of charge from The Cambridge Crystallographic Data Centre via www.ccdc.cam.ac.uk/data_request/cif.

Crystallographic data for **DT-P** (**3**): crystal size: 0.30×0.06×0.04 mm^3; monoclinic; $C2/c$; Z=4; a=21.662 (4) Å, b=4.0056 (8) Å, c=21.773 (4) Å; V=1673.5 (6) $Å^3$; $\rho_{calculated}$=1.455 g cm^{-3}; of 6396 reflections, 2003 were unique; GOF=1.124; 132 parameters; $R1$=0.0638, $wR2$=0.1516 (for all reflections).

Crystallographic data for **DTz-P** (**4**): 0.30×0.20×0.05 mm^3; monoclinic; $P2(1)/n$; Z=2; a=3.8727 (8) Å, b=20.191 (4) Å, c=10.540 (2) Å; V=812.9 (3) $Å^3$; $\rho_{calculated}$=1.505 g cm^{-3}; of 6446 reflections, 1828 were unique; GOF=1.180; 155 parameters; $R1$=0.0871, $wR2$=0.1639 (for all reflections).

Crystallographic data for **DPh-P** (**5**): 0.29×0.27×0.24 mm^3; orthorhombic; $Pbca$; Z=4; a=7.7673 (16) Å, b=7.6033 (15) Å, c=30.732 (6) Å; V=1815.0 (6) $Å^3$; $\rho_{calculated}$=1.297 g cm^{-3}; of 10,002 reflections, 1647 were unique; GOF=1.348; 127 parameters; $R1$=0.0743, $wR2$=0.1818 (for all reflections).

Crystallographic data for **DHT-P** (**6**): 0.37×0.29×0.10 mm^3; triclinic; P–1; Z=1; a=5.727 (2) Å, b=7.821 (4) Å, c=16.117 (7) Å; V=699.5 (5) $Å^3$; $\rho_{calculated}$=1.270 g cm^{-3}; of 9284 reflections, 3185 were unique; GOF=1.079; 173 parameters; $R1$=0.0562, $wR2$=0.1314 (for all reflections).

4.4. FET device fabrication and measurement

OFET devices based on vacuum-deposited thin films were fabricated in a top-contact device configuration. The heavily doped n-type Si wafer with a 500 nm-thick SiO_2 layer and a capacitance of 7.5 nF cm^{-2} was used as the substrate. The gate dielectric was treated with octadecyltrichlorosilane (OTS) by a vapor deposition method. All materials (**3**, **5**, and **6**) were deposited on substrates by thermal evaporation under a pressure of 4–6×10^{-4} Pa at a deposition rate gradually increased from 0.1 Å s^{-1} to 0.5 Å s^{-1} at the first 10 nm and then maintained until the thickness of the film was 50 nm. The deposition rate and film thickness were monitored by ULVAC CRTM-6000. Subsequently, 20 nm thick gold source and drain electrodes were deposited on the films via a shadow mask. The channel length and width were 0.11 mm and 5.30 mm, respectively. The FET characteristics were measured at room temperature in air using Keithley 4200 SCS.

4.5. Physicochemical studies

UV–vis spectra were recorded on a JASCO V-570 spectrometer. Cyclic voltammetry (CV) measurements were carried out on a CHI660C analyzer in a conventional three-electrode cell setup with Pt button as the working electrode, a platinum wire as the counter electrode, Ag/AgCl as the reference electrode and calibrated with ferrocene/ferrocenium (Fc/Fc^+) as an external potential marker in anhydrous CH_2Cl_2 solution containing 0.1 M $^nBu_4NPF_6$ as a supporting electrolyte at a scan rate of 100 mV s^{-1} under a nitrogen atmosphere at room temperature. Thermal gravimetric analysis (TGA) was performed on a Shimadzu DTG 60 instrument. X-ray diffraction (XRD) measurements of thin films were performed in reflection mode at 40 kV and 200 mA with Cu Kα radiation using a 2 kW Rigaku X-ray diffractometer. Atomic force microscopy (AFM) images of the thin films were obtained on a Nanoscope IIIa AFM (Digital Instruments) operating in tapping mode.

Acknowledgements

The authors acknowledge the financial support from National Natural Science Foundation of China (21021091, 20952001), Ministry of Science and Technology of China, and Chinese Academy of Sciences.

Supplementary data

These data include TGA and DSC for compounds **3**–**6**, X-ray crystallographic analyses for compounds **3** (CCDC 808315), **4** (CCDC 808316), **5** (CCDC 808317), **6** (CCDC 808318), OFETs characteristic curves for compound **3**, **5**, and **6**, copies of ^1H and ^{13}C NMR spectra and for compounds **3**–**6**. Supplementary data related to this article can be found online at doi:10.1016/j.tet.2011.03.055.

References and notes

1. Kelley, T. W.; Baude, P. F.; Gerlach, C.; Ender, D. E.; Muyres, D.; Haase, M. A.; Vogel, D. E.; Theiss, S. D. *Chem. Mater.* **2004**, *16*, 4413.
2. Mas-Torrent, M.; Rovira, C. *Chem. Soc. Rev.* **2008**, *37*, 827.
3. Allard, S.; Forster, M.; Souharce, B.; Thiem, H.; Scherf, U. *Angew. Chem., Int. Ed.* **2008**, *47*, 4070.
4. Tsumura, A.; Koezuka, H.; Ando, T. *Appl. Phys. Lett.* **1986**, *49*, 1210.
5. Chen, J. L.; Leblanc, V.; Kang, S. H.; Benning, P. J.; Schut, D.; Baldo, M. A.; Schmidt, M. A.; Bulovic, V. *Adv. Funct. Mater.* **2007**, *17*, 2722.
6. Dimitrakopoulos, C. D.; Malenfant, P. R. L. *Adv. Mater.* **2002**, *14*, 99.
7. Forrest, S. R. *Chem. Rev.* **1997**, *97*, 1793.
8. Coropceanu, V.; Cornil, J.; da Silva, D. A.; Olivier, Y.; Silbey, R.; Bredas, J. L. *Chem. Rev.* **2007**, *107*, 926.
9. Murphy, A. R.; Frechet, J. M. J. *Chem. Rev.* **2007**, *107*, 1066.
10. Zaumseil, J.; Sirringhaus, H. *Chem. Rev.* **2007**, *107*, 1296.
11. Baca, A. J.; Ahn, J. H.; Sun, Y. G.; Meitl, M. A.; Menard, E.; Kim, H. S.; Choi, W. M.; Kim, D. H.; Huang, Y.; Rogers, J. A. *Angew. Chem., Int. Ed.* **2008**, *47*, 5524.
12. Voss, D. *Nature* **2000**, *407*, 442.
13. Crone, B.; Dodabalapur, A.; Lin, Y. Y.; Filas, R. W.; Bao, Z.; LaDuca, A.; Sarpeshkar, R.; Katz, H. E.; Li, W. *Nature* **2000**, *403*, 521.
14. Mitschke, U.; Bauerle, P. *J. Mater. Chem.* **2000**, *10*, 1471.
15. Andersson, P.; Forchheimer, R.; Tehrani, P.; Berggren, M. *Adv. Funct. Mater.* **2007**, *17*, 3074.

16. Sheraw, C. D.; Zhou, L.; Huang, J. R.; Gundlach, D. J.; Jackson, T. N.; Kane, M. G.; Hill, I. G.; Hammond, M. S.; Campi, J.; Greening, B. K.; Francl, J.; West, J. *Appl. Phys. Lett.* **2002**, *80*, 1088.
17. Huitema, H. E. A.; Gelinck, G. H.; van der Putten, J. B. P. H.; Kuijk, K. E.; Hart, C. M.; Cantatore, E.; Herwig, P. T.; van Breemen, A. J. J. M.; de Leeuw, D. M. *Nature* **2001**, *414*, 599.
18. Crone, B. K.; Dodabalapur, A.; Sarpeshkar, R.; Gelperin, A.; Katz, H. E.; Bao, Z. *J. Appl. Phys.* **2002**, *91*, 10140.
19. Lin, Y. Y.; Dodabalapur, A.; Sarpeshkar, R.; Bao, Z.; Li, W.; Baldwin, K.; Raju, V. R.; Katz, H. E. *Appl. Phys. Lett.* **1999**, *74*, 2714.
20. Klauk, H.; Halik, M.; Zschieschang, U.; Schmid, G.; Radlik, W.; Weber, W. *J. Appl. Phys.* **2002**, *92*, 5259.
21. Nelson, S. F.; Lin, Y. Y.; Gundlach, D. J.; Jackson, T. N. *Appl. Phys. Lett.* **1998**, *72*, 1854.
22. Anthony, J. E.; Eaton, D. L.; Parkin, S. R. *Org. Lett.* **2002**, *4*, 15.
23. Sheraw, C. D.; Jackson, T. N.; Eaton, D. L.; Anthony, J. E. *Adv. Mater.* **2003**, *15*, 2009.
24. Tang, M. L.; Okamoto, T.; Bao, Z. N. *J. Am. Chem. Soc.* **2006**, *128*, 16002.
25. Tang, M. L.; Mannsfeld, S. C. B.; Sun, Y. S.; Becerril, H. A.; Bao, Z. N. *J. Am. Chem. Soc.* **2009**, *131*, 882.
26. Yan, Q.; Zhou, Y.; Ni, B. B.; Ma, Y. G.; Wang, J.; Pei, J.; Cao, Y. *J. Org. Chem.* **2008**, *73*, 5328.
27. Shukla, D.; Welter, T. R.; Robello, D. R.; Giesen, D. J.; Lenhard, J. R.; Ahearn, W. G.; Meyer, D. M.; Rajeswaran, M. *J. Phys. Chem. C* **2009**, *113*, 14482.
28. Winnik, F. M. *Chem. Rev.* **1993**, *93*, 587.
29. Zhang, H. J.; Wang, Y.; Shao, K. Z.; Liu, Y. Q.; Chen, S. Y.; Qiu, W. F.; Sun, X. B.; Qi, T.; Ma, Y. Q.; Yu, G.; Su, Z. M.; Zhu, D. B. *Chem. Commun.* **2006**, 755.
30. Ashizawa, M.; Yamada, K.; Fukaya, A.; Kato, R.; Hara, K.; Takeya, J. *Chem. Mater.* **2008**, *20*, 4883.
31. Wang, Y.; Wang, H. M.; Liu, Y. Q.; Di, C. A.; Sun, Y. M.; Wu, W. P.; Yu, G.; Zhang, D. Q.; Zhu, D. B. *J. Am. Chem. Soc.* **2006**, *128*, 13058.
32. Coventry, D. N.; Batsanov, A. S.; Goeta, A. E.; Howard, J. A. K.; Marder, T. B.; Perutz, R. N. *Chem. Commun.* **2005**, 2172.
33. Shinamura, S.; Miyazaki, E.; Takimiya, K. *J. Org. Chem.* **2010**, *75*, 1228.
34. Cornil, J.; Calbert, J. P.; Bredas, J. L. *J. Am. Chem. Soc.* **2001**, *123*, 1250.
35. Facchetti, A.; Yoon, M. H.; Stern, C. L.; Hutchison, G. R.; Ratner, M. A.; Marks, T. J. *J. Am. Chem. Soc.* **2004**, *126*, 13480.
36. Thelakkat, M.; Schmidt, H. W. *Adv. Mater.* **1998**, *10*, 219.
37. Frisch, M. J.; Trucks, G. W.; Schlegel, H. B.; Scuseria, G. E.; Robb, M. A.; Cheeseman, J. R.; Montgomery, J. A., Jr.; Vreven, T.; Kudin, K. N.; Burant, J. C.; Millam, J. M.; Iyengar, S. S.; Tomasi, J.; Barone, V.; Mennucci, B.; Cossi, M.; Scalmani, G.; Rega, N.; Petersson, G. A.; Nakatsuji, H.; Hada, M.; Ehara, M.; Toyota, K.; Fukuda, R.; Hasegawa, J.; Ishida, M.; Nakajima, T.; Honda, Y.; Kitao, O.; Nakai, H.; Klene, M.; Li, X.; Knox, J. E.; Hratchian, H. P.; Cross, J. B.; Adamo, C.; Jaramillo, J.; Gomperts, R.; Stratmann, R. E.; Yazyev, O.; Austin, A. J.; Cammi, R.; Pomelli, C.; Ochterski, J. W.; Ayala, P. Y.; Morokuma, K.; Voth, G. A.; Salvador, P.; Dannenberg, J. J.; Zakrzewski, V. G.; Dapprich, S.; Daniels, A. D.; Strain, M. C.; Farkas, O.; Malick, D. K.; Rabuck, A. D.; Raghavachari, K.; Foresman, J. B.; Ortiz, J. V.; Cui, Q.; Baboul, A. G.; Clifford, S.; Cioslowski, J.; Stefanov, B. B.; Liu, G.; Liashenko, A.; Piskorz, P.; Komaromi, I.; Martin, R. L.; Fox, D. J.; Keith, T.; Al-Laham, M. A.; Peng, C. Y.; Nanayakkara, A.; Challacombe, M.; Gill, P. M. W.; Johnson, B.; Chen, W.; Wong, M. W.; Gonzalez, C.; Pople, J. A. *Gaussian 03, Version C02*; Gaussian: Wallingford, CT, 2004.